Can Observation Targeting Be a Wild Goose Chase? An Adjoint-Sensitivity Study of a U.S. East Coast Cyclone Forecast Bust

DANIEL J. LLOVERAS,[a,b] JAMES D. DOYLE,[c] AND DALE R. DURRAN[a]

[a] *Department of Atmospheric Sciences, University of Washington, Seattle, Washington*
[b] *National Research Council, Monterey, California*
[c] *U.S. Naval Research Laboratory, Monterey, California*

(Manuscript received 6 March 2024, in final form 14 October 2024, accepted 6 December 2024)

ABSTRACT: Efforts to improve midlatitude-cyclone forecasts by deploying supplemental observations in localized target regions often fall short of expectations. We consider a potential contributing factor to these underwhelming results by investigating the initial-condition sensitivity of the 15 November 2018 East Coast cyclone forecast bust. We use a moist adjoint model to compute the initial-condition perturbations that minimize the large 48–72-h synoptic-scale forecast errors associated with this storm. The adjoint-optimal perturbations, which have maximum amplitudes of about 2 K in temperature and 1 m s^{-1} in horizontal wind speed, are widespread, extending throughout the troposphere and along a ridge–trough pattern covering much of North America. We investigate the most impactful components of the perturbations by truncating them in physical and spectral space and rescaling them to be equal in a domain-integrated energy norm to the full, unmodified perturbations. When the perturbations are confined to a localized target region of strongest sensitivity, they have weaker impacts on the forecast than when the perturbations within the target region are removed and the rest of the perturbations are retained. Additionally, when the perturbations are filtered to retain only wavelengths longer than 1000 km, they have stronger impacts on the forecast than when the perturbations are filtered to retain only wavelengths shorter than 1000 km. These results suggest that midlatitude-cyclone forecast improvements from targeted observations can be overwhelmed by smaller-amplitude but widespread and large-scale initial-condition sensitivities outside of the target region.

SIGNIFICANCE STATEMENT: Poor forecasts of midlatitude cyclones can cause tremendous socioeconomic disruption via unexpected heavy precipitation and damaging winds. One approach to improving these forecasts involves targeting observations in localized regions where initial-condition errors are expected to be most harmful to forecast accuracy. These efforts are expensive, yet they typically produce only minor forecast improvements. By examining a recent poorly forecast midlatitude cyclone, we find that a potential contributing factor to these underwhelming results is that small, but widespread changes to the initial state can be more impactful than the big, but localized changes that targeting is designed to make. This suggests that efforts to reduce initial-condition errors over broad areas can be more economical for improving midlatitude-cyclone forecasts than targeted observations.

KEYWORDS: Extratropical cyclones; Sensitivity studies; Numerical weather prediction/forecasting

1. Introduction

Present-day numerical weather prediction (NWP) models routinely produce accurate forecasts of midlatitude cyclones about 1 week in advance (Hoskins 2013; Bauer et al. 2015), but there are occasional "forecast busts" with unusually poor skill even at shorter 2–3-day lead times. Since the rapid growth of initial-condition errors can play a predominant role in these events (Magnusson et al. 2019), one approach to mitigate forecast busts is to improve the analysis with additional "targeted" observations. Also known as adaptive sampling, observation targeting involves deploying supplemental observations (typically with rawinsondes or dropwindsonde-equipped aircraft) to regions where initial-condition errors are expected to be most detrimental to forecast accuracy. Target regions can be objectively identified either by estimating the sensitivity of the forecast to the initial state with tools like adjoint models (Langland et al. 1999a) and singular vectors (Palmer et al. 1998), or by estimating the impact of additional observations on the forecast with tools like the ensemble transform Kalman filter (Bishop et al. 2001) and the forecast sensitivity to observations method (Langland and Baker 2004). For midlatitude cyclones, the different techniques usually identify similar meso- to synoptic-scale target regions along baroclinic zones (Majumdar 2016), although there are sometimes substantial differences, especially at smaller scales (Majumdar et al. 2002a; Ancell and Hakim 2007).

In the late 1990s, the Fronts and Atlantic Storm Track Experiment (FASTEX; Joly et al. 1999) and the North Pacific Experiment (NORPEX; Langland et al. 1999b) demonstrated that real-time observation targeting for midlatitude cyclones is practicable. The forecast improvements were also promising, with 10%–15% error reductions for several modeling systems and cases (Langland 2005). However, more recent results have been less encouraging. For example, Hamill et al. (2013) determined that targeted observations from the Winter Storm Reconnaissance (WSR) program in 2011 had generally neutral forecast impacts, contributing to the suspension of that program in 2014. Also, targeting efforts during The

---

Corresponding author: Daniel J. Lloveras, daniel.j.lloveras.ctr@us.navy.mil

DOI: 10.1175/JAS-D-24-0044.1

© 2025 American Meteorological Society. This published article is licensed under the terms of the default AMS reuse license. For information regarding reuse of this content and general copyright information, consult the AMS Copyright Policy (www.ametsoc.org/PUBSReuseLicenses).

Brought to you by NAVAL RESEARCH LABORATORY | Unauthenticated | Downloaded 02/06/25 06:40 PM UTC

Observing Research and Predictability Experiment (THORPEX) from 2005 to 2014 and the North Atlantic Waveguide and Downstream Impact Experiment (NAWDEX) in 2016 had generally positive but marginal forecast impacts (Majumdar 2016; Schindler et al. 2020).

Despite these underwhelming results, research and field efforts on targeted observations have continued. Since it has been proposed that improvements to NWP models, data assimilation systems, and routinely available observations since the late 1990s have led to the drop-off in targeting impacts, observing system simulation experiments have been conducted to determine whether there is still room for benefit from targeted observations. For example, Peevey et al. (2018) determined that there was still room for 5%–15% error reductions from targeted observations for three winter storms impacting the West Coast of the United States. It has also been proposed that conventional rawinsondes and aircraft observations are unable to sufficiently sample target areas, so other observing platforms like high-altitude, long-endurance uncrewed aircraft have been explored (Wick et al. 2020). Outside of midlatitude cyclones, targeting campaigns have continued for smaller-scale atmospheric phenomena like mesoscale convective systems (Hill et al. 2021), tropical cyclones (Sippel et al. 2022), and atmospheric rivers (Lord et al. 2022), typically with more encouraging results.

Given the high cost, minimal forecast improvements, and continuation of observation targeting for midlatitude cyclones, it is worth investigating why these efforts often fall short of expectations. In addition to the aforementioned hypotheses regarding room for improvement and observation type, one idea is that initial-condition sensitivities are often too widespread to be targeted for observation. For example, Langland et al. (2002) used a dry adjoint model with 150-km grid spacing to compute the initial-condition perturbations that minimized 72-h forecast errors for the 25 January 2000 “surprise” snowstorm. They found that these perturbations extended over large swaths of North America and the northeastern Pacific, suggesting that deploying targeted observations to a specific region would not have been a practical approach to mitigate this forecast bust. Despite this result, and the consensus that sensitive regions are often too large in scale to be completely covered by a single aircraft mission (Majumdar 2016), efforts have still been made to target the highest-amplitude components of sensitivity patterns, which tend to be more localized (e.g., Majumdar et al. 2002b, their Fig. 2). However, our hypothesis is that, in these cases, the benefits of reducing initial-condition errors over a localized region of strongest sensitivity can be overwhelmed by smaller-amplitude but widespread sensitivities outside of the target region, rendering the overall impact of targeted observations on the forecast minimal. To the best of our knowledge, no other study has considered this as a potential contributing factor to the often-underwhelming results from targeted observations for midlatitude cyclones.

The goal of this paper is to test our hypothesis on a midlatitude cyclone that impacted the East Coast of the United States on 15 November 2018. We use this event for our case study because NWP models struggled to accurately forecast the cyclone’s location and intensity even at relatively short 2–3-day lead times, which contributed to poor operational forecasts of its accompanying snowfall and led to substantial societal disruption (Novak et al. 2023). A synoptic overview of this storm is provided in section 2. The methods are in section 3. Similar to Langland et al. (2002), our strategy is to compute the initial-condition perturbations that minimize the 48–72-h errors associated with this forecast bust, but our adjoint model incorporates moist physics and is run with a much finer 30-km grid spacing. In section 4, we discuss the structure and impact of the perturbations. To test our hypothesis about targeting, we compare the impact of the perturbations when they are confined to or removed from localized regions of strongest sensitivity, as well as when they are filtered to retain only short or long wavelengths. In section 5, we investigate the initial-condition sensitivity using the same sets of perturbations but evolved with a convection-permitting model. The conclusions are in section 6.

2. Synoptic overview

Figure 1 shows the Global Forecast System (GFS) analysis for 500-hPa geopotential height and sea level pressure over the 72-h period from 1200 UTC 13 to 1200 UTC 16 November 2018. At the beginning of this period, a positively tilted upper-level trough was oriented over the central United States, and surface high pressure was present over much of the contiguous United States (Fig. 1a). Over the next 24 h, a closed upper-level low detached from the longwave trough, and the trough propagated eastward in association with a surface cyclone exiting to the northeast (Fig. 1b). Meanwhile, the surface high pressure extended northeastward, resulting in cool northerly flow throughout much of the northeastern United States. The upper-level cutoff low then moved northeastward slowly and deepened slightly, and a closed surface low formed along the Kentucky–Tennessee border by 1200 UTC 15 November 2018 (Fig. 1c). This surface low dissipated over the Appalachian Mountains as the upper-level cutoff low moved toward the Mid-Atlantic Coast, a region with strong low-level baroclinity due to the warm Gulf Stream waters and cold air dammed east of the Appalachian Mountains after the previous day’s northerly flow. Consequently, the inverted trough off the coasts of North and South Carolina at 1200 UTC 15 November 2018 developed into a midlatitude cyclone that brought early season snowfall to parts of the northeastern United States on the evening of 15 November 2018 and early morning of 16 November 2018. The surface cyclone deepened to 995 hPa by 1200 UTC 16 November 2018, and the upper-level cutoff low was ingested back into the longwave pattern (Fig. 1d). This case was an example of a “Miller Type-B” storm in which a surface cyclone dissipates over the Appalachian Mountains and a more intense cyclone develops along the East Coast due to the strong low-level baroclinity in that region (Miller 1946).

The deterministic GFS exhibited substantial errors in forecasting the evolution of the upper-level cutoff low and the ensuing surface cyclone. Figure 2a shows that the GFS forecast initialized at 1200 UTC 13 November 2018 had the cutoff low

Brought to you by NAVAL RESEARCH LABORATORY | Unauthenticated | Downloaded 02/06/25 06:40 PM UTC

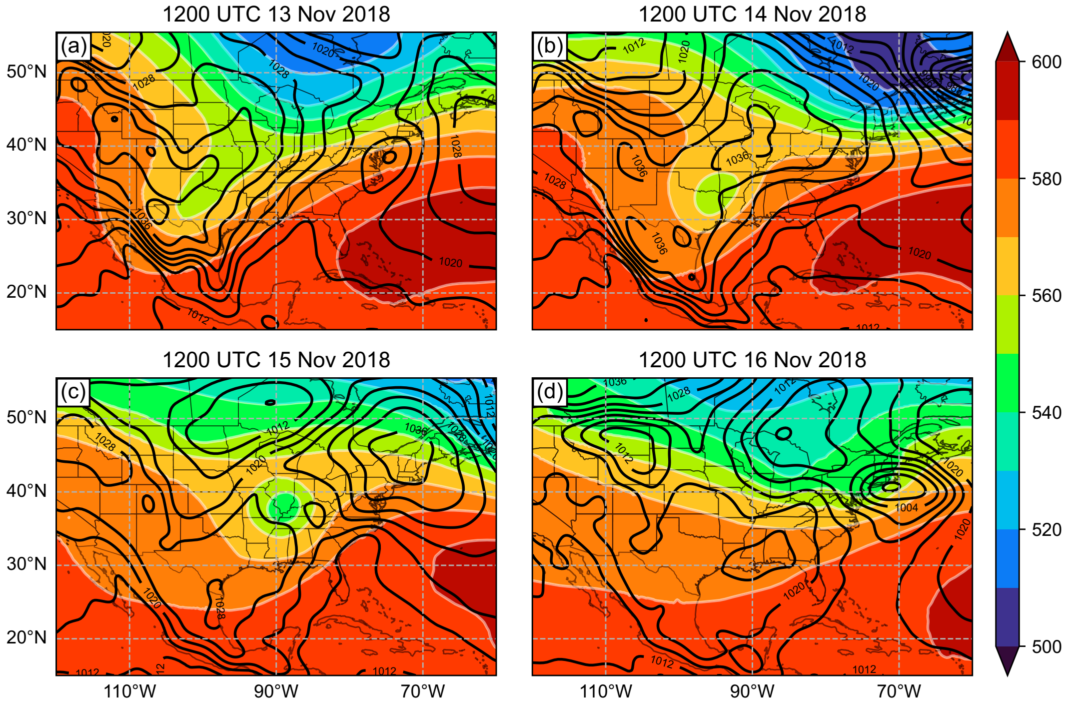

FIG. 1. GFS analysis for sea level pressure (black contours every 4 hPa) and 500-hPa geopotential height (color fill every 10 dam) at (a) 1200 UTC 13 Nov 2018, (b) 1200 UTC 14 Nov 2018, (c) 1200 UTC 15 Nov 2018, and (d) 1200 UTC 16 Nov 2018.

too far south compared to the analysis, with errors greater than 100 m in 500-hPa geopotential height at just a 48-h lead time. These height errors were even greater than those at similar lead times in the medium-range European bust cases analyzed by Magnusson (2017). Figure 2b shows that this GFS forecast also had the surface cyclone too far south (and too weak) compared to the analysis at a 72-h lead time. At 1200 UTC 16 November 2018, the analysis had the low just east of Long Island with a minimum central pressure of 995 hPa, whereas the forecast had the low further south near New Jersey

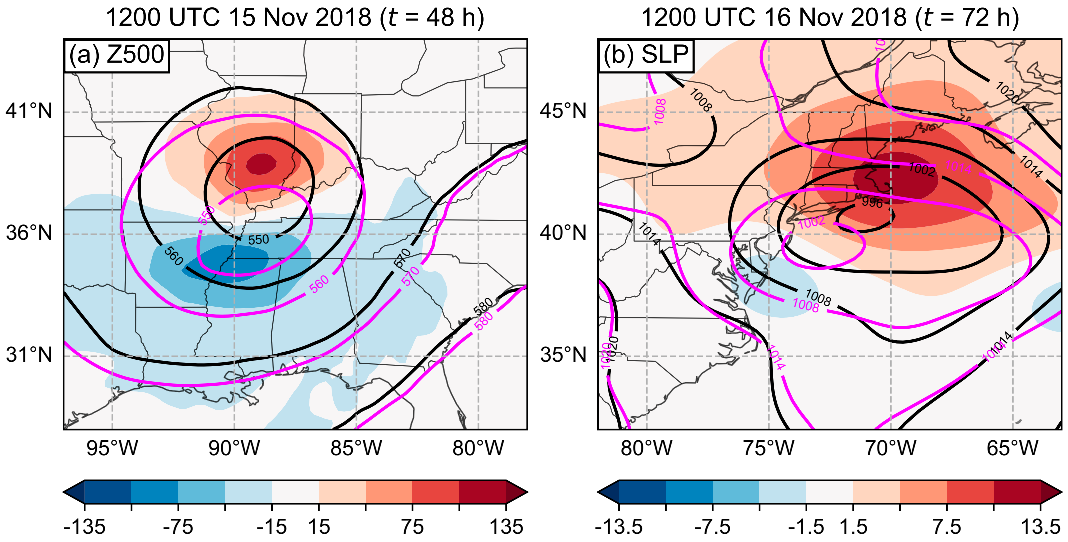

FIG. 2. (a) 48-h errors in 500-hPa geopotential height (Z500) and (b) 72-h errors in sea level pressure (SLP) for the GFS forecast initialized at 1200 UTC 13 Nov 2018. The GFS analysis (black) and forecast (magenta) are contoured every 10 dam for Z500 and every 6 hPa for SLP. The forecast minus the analysis (color fill) is contoured every 30 m for Z500 and every 3 hPa for SLP.

Brought to you by NAVAL RESEARCH LABORATORY | Unauthenticated | Downloaded 02/06/25 06:40 PM UTC

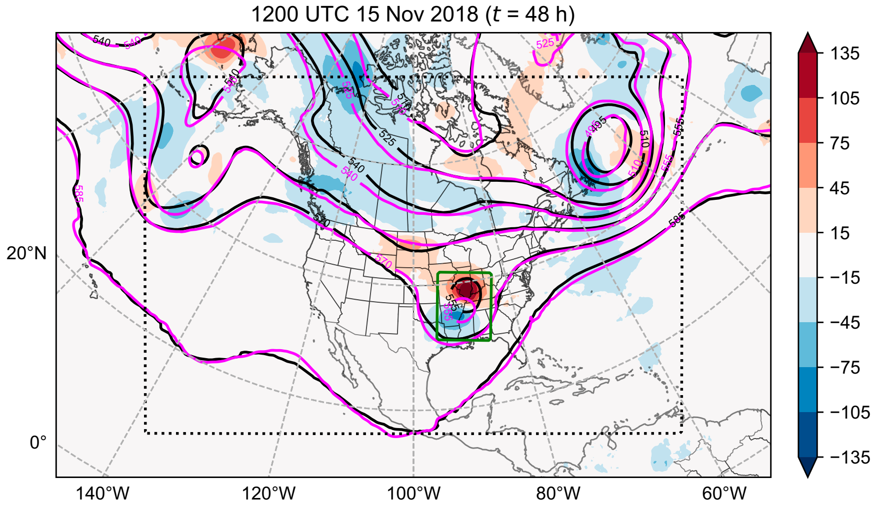

1200 UTC 15 Nov 2018 (t = 48 h)

FIG. 3. 48-h forecast errors in 500-hPa geopotential height for the 30-km WRF simulation. The GFS analysis (black) and WRF forecast (magenta) are contoured every 15 dam. The forecast minus the analysis (color fill) is contoured every 30 m. The full extent of the WRF domain is plotted. The dotted black line shows the extent of the COAMPS domain. The green contour bounds the response-function region used to compute the adjoint perturbations.

with a minimum central pressure of 1001 hPa, amounting to errors in sea level pressure of about 12 hPa. The unusually poor model guidance for this midlatitude cyclone contributed to poor operational forecasts for its accompanying snowfall. In particular, the National Weather Service predicted just 1–2 in. of snowfall for New York City, but more than 6 in. fell, breaking numerous daily records and shutting down travel in the city (Novak et al. 2023). Although here we have focused on the performance of the deterministic GFS, appendix A shows that this event was also a forecast bust for ensemble forecasting systems and for different global NWP models.

Given these large synoptic-scale errors, our focus is on the sensitivity of the 48-h forecast for the upper-level cutoff low to the initial conditions at 1200 UTC 13 November 2018. We also consider the effects of this sensitivity on the 72-h forecast for the surface cyclone.

3. Methods

a. Nonlinear model

We use the Advanced Research version of Weather Research and Forecasting Model (WRF-ARW, version 4.4; Skamarock et al. 2021) to run the nonlinear numerical simulations of this storm over the 72-h period from 1200 UTC 13 to 1200 UTC 16 November 2018. We run two sets of simulations: one with parameterized convection and the other with explicit convection.

The simulations with parameterized convection have a Lambert conformal conic projection for the horizontal domain with 30-km grid spacing, 400 × 250 grid points, a center grid point at 45°N, 100°W, and true latitudes at 20° and 70°N. Figure 3 shows the full extent of this domain, which covers the entirety of North America and large portions of the northeast Pacific and northwest Atlantic. There are 45 staggered vertical levels with a model top at 50 hPa and the Rayleigh damping scheme from Klemp et al. (2008) in the top 5 km to prevent gravity wave reflections. Other model physics include the Thompson microphysics scheme (Thompson et al. 2008), the Tiedtke cumulus scheme (Tiedtke 1989; Zhang et al. 2011), the Noah land surface model (Tewari et al. 2004), the Mellor–Yamada–Janjić (MYJ) planetary-boundary-layer and surface-layer schemes (Janjić 1994), and the Rapid Radiative Transfer Model for global climate models (RRTMG) for longwave and shortwave radiation. The initial conditions come from the GFS analysis at 1200 UTC 13 November 2018, and the GFS forecast initialized at this time is used to update the lateral boundary conditions every 3 h. Figure 3 shows that the 30-km WRF forecast for 500-hPa geopotential height is similar to the GFS forecast at a 48-h lead time (Fig. 2a), with the cutoff low well south of the analysis.

For the simulations with explicit convection, all of the settings are the same except the grid spacing is 4 km, there are 3000 × 1875 grid points, there are 60 staggered vertical levels, and there is no cumulus parameterization. Additionally, we initialize the model at 0900 UTC 13 November 2018 to allow for a 3-h spinup period due to the downscaling of the coarser-resolution initial conditions. The solution does not diverge much from the analysis over this 3-h period (not shown), so for the initial-condition perturbation experiments discussed in section 5, we add the perturbations at the same time as in the experiments with parameterized convection (i.e., at 1200 UTC 13 November 2018).

b. Tangent-linear and adjoint models

Adjoint models (Errico 1997) are powerful tools for quantifying the influence of each component of the initial

Brought to you by NAVAL RESEARCH LABORATORY | Unauthenticated | Downloaded 02/06/25 06:40 PM UTC

model state $\mathbf{x}_0$ on a scalar aspect J of the model state at a later time $\mathbf{x}_t$,

$$J(\mathbf{x}_t) = J[M(\mathbf{x}_0)], \tag{1}$$

where M is the nonlinear model. The scalar J is commonly referred to as the response function. The sensitivity of the response function to changes in the initial state can be estimated by

$$\frac{\partial J}{\partial \mathbf{x}_0} = \mathbf{M}_{0,t}^{\mathrm{T}} \frac{\partial J}{\partial \mathbf{x}_t}, \tag{2}$$

where the tangent-linear model $\mathbf{M}_{0,t}$ is obtained by linearizing M at each time step along a reference nonlinear trajectory from the initial time to the final time. The transpose of the tangent-linear model $\mathbf{M}_{0,t}^{\mathrm{T}}$ is the adjoint model, and it maps the gradient of J with respect to the final state to the gradient of J with respect to the initial state.

The adjoint-sensitivity gradient $\partial J/\partial \mathbf{x}_0$ expresses the impact of a unit change to each initial-state variable on the response function. However, it is often more physically meaningful to express the sensitivity fields as "optimal" perturbations to the initial conditions that either minimize or maximize J subject to some scaling. Such scaling is necessary to satisfy the tangent-linear approximation that perturbations evolved by $\mathbf{M}_{0,t,}$ are similar in magnitude and spatial pattern to those evolved by M. The perturbations can also be scaled so that they are comparable in magnitude to analysis errors in real-world data assimilation systems.

In this paper, we compute adjoint-derived optimal perturbations following Doyle et al. (2014, 2019). Changes to J are expressed as

$$J' = \sum_{m,j} \frac{\partial J}{\partial x_{m,j}} x'_{m,j}, \tag{3}$$

where $\partial J/\partial x_{m,j}$ is the adjoint-sensitivity gradient of the response function with respect to the initial value of variable m at grid point j and $x'_{m,j}$ are the adjoint perturbations. We define $x'_{m,j}$, for each prognostic variable as

$$x'_{m,j} = \frac{s}{w_m} \frac{\partial J}{\partial x_{m,j}}. \tag{4}$$

The perturbed prognostic variables are the zonal, meridional, and vertical wind components; potential temperature; perturbation pressure; and water vapor mixing ratio. These variables have different relative magnitudes (e.g., 1 K is a small change in potential temperature, but 1 kg kg^{-1} is a huge change in water vapor mixing ratio), so the perturbations are weighted by the domain-maximum forecast differences for each variable m over the integration period:

$$w_m = [\max_j(|x_t^m - x_0^m|)]^{-2}. \tag{5}$$

Finally, the scaling parameter s is defined such that the maximum perturbation for wind, potential temperature, or water vapor does not exceed 1 m s^{-1}, 1 K, or 1 g kg^{-1}, respectively. The perturbations are optimal in the sense that they produce the greatest (positive or negative) change to the response function as expressed by (3) for the smallest-amplitude perturbations subject to the constraint imposed by the scaling parameter s in (4).

To compute the adjoint-derived optimal perturbations for the 15 November 2018 forecast bust, we would ideally use the adjoint model for WRF (Zhang et al. 2013), but the code is built within WRF's four-dimensional variational data assimilation module, so there is no user interface for stand-alone adjoint runs. Instead, we use the adjoint of the atmospheric module of the Coupled Ocean–Atmosphere Mesoscale Prediction System (COAMPS; Amerault et al. 2008).

Our COAMPS domain is nearly identical to that of the WRF runs with parameterized convection, with the same Lambert conformal conic projection and 30-km horizontal grid spacing. However, we use a smaller domain size with 301 × 201 grid points due to computational constraints and potential instabilities in the adjoint model associated with large variations in the map scale factor. This smaller domain is indicated by the dotted black line in Fig. 3. As in the WRF runs with parameterized convection, we use the GFS analysis at 1200 UTC 13 November 2018 for the initial conditions and the GFS forecast initialized at that time for the lateral boundary conditions.

Model physics closely follow those of Doyle et al. (2014, 2019) and include a modified version of the Rutledge and Hobbs (1983) microphysics scheme, a modified Kuo convective parameterization (Molinari 1985), a turbulent kinetic energy budget to parameterize turbulent mixing and diffusion processes in the boundary layer and free atmosphere (Hodur 1997), and a modified version of the Louis (1979) surface-layer parameterization. The tangent-linear and adjoint models use the same physics parameterizations as the nonlinear COAMPS model, but gradients and perturbations associated with vertical diffusion are neglected following Mahfouf (1999). There are 45 vertical levels with a model top at 30 km and a sponge upper-boundary condition over the top 10 km to prevent gravity wave reflections.

c. *Diagnostic forecast correction via iterative adjoint computations*

Our goal in using the adjoint model is to compute the initial-condition perturbations that minimize the 48-h forecast errors for the upper-level cutoff low. Thus, we define the response function J as the squared difference between the forecast potential vorticity (PV) and the analysis PV at 1200 UTC 15 November 2018 averaged over a region containing the cutoff low. The horizontal extent of this region is marked by the green contour in Fig. 3, and it extends vertically between the model levels closest to 500 and 300 hPa.

Starting from the nonlinear COAMPS simulation with GFS-analysis initial conditions $\mathbf{x}_0$, we use the adjoint model to compute the perturbations $\delta\mathbf{x}_0^{(1)}$ that produce the greatest tangent-linear decrease in J following the procedure described

Brought to you by NAVAL RESEARCH LABORATORY | Unauthenticated | Downloaded 02/06/25 06:40 PM UTC

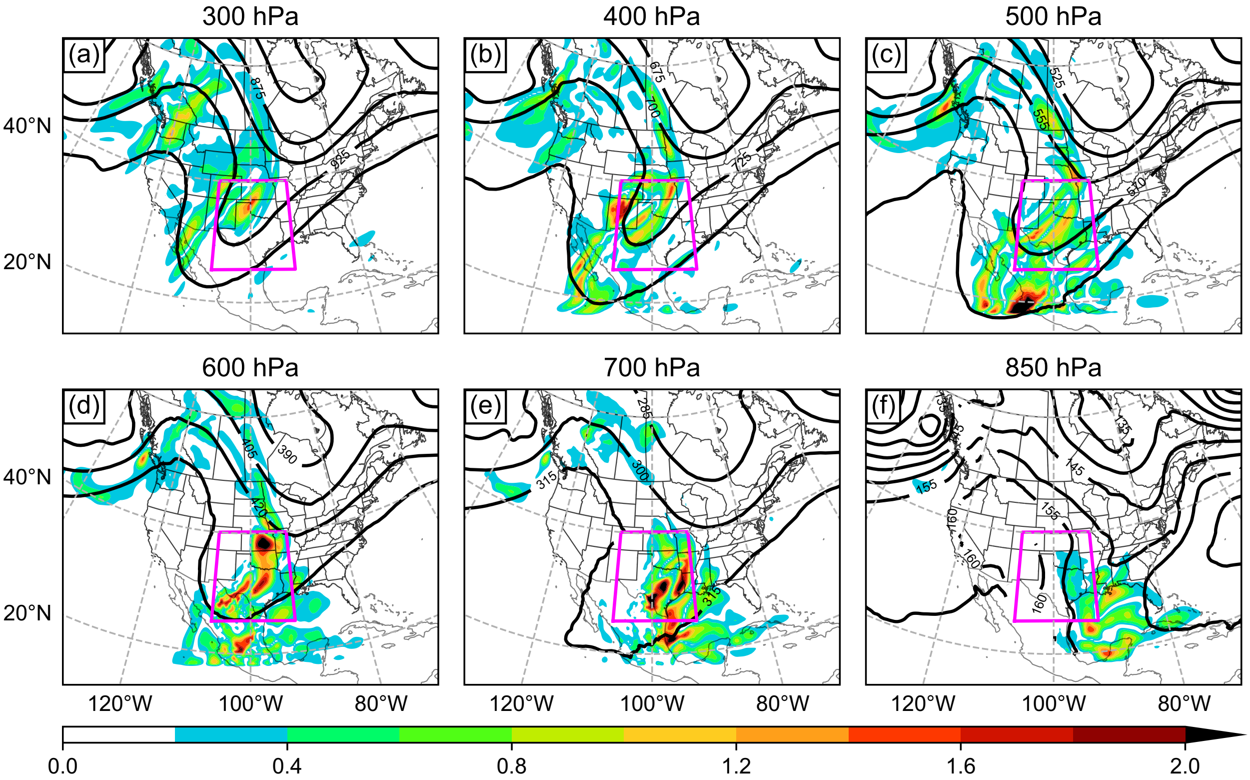

FIG. 4. Square root of the DTE of the adjoint-derived perturbations (color fill every 0.2 m s^{-1}) and GFS analysis for geopotential height (black contours in dam) at 1200 UTC 13 Nov 2018 and at (a) 300, (b) 400, (c) 500, (d) 600, (e) 700, and (f) 850 hPa. The magenta contours bound the target region.

in section 3b. These perturbations are then added to obtain the initial conditions for a new nonlinear run:

$$\mathbf{x}_0^{(1)} = \mathbf{x}_0 + \delta\mathbf{x}_0^{(1)}. \tag{6}$$

The nonlinear forecast starting from $\mathbf{x}_0^{(1)}$ produces a cutoff low that is closer to the analysis than the original forecast, but J can be reduced even further by using a new adjoint run to compute the optimal perturbations $\delta\mathbf{x}_0^{(2)}$ corresponding to the improved nonlinear trajectory. This procedure is then iterated to minimize J in a manner broadly analogous to the iterative cost-function minimization in variational data assimilation. Previous studies have used similar iterative adjoint methods to obtain the diagnostic initial-condition perturbations that correct forecast busts (Klinker et al. 1998; Langland et al. 2002; Kleist and Morgan 2005), although each of these studies used dry adjoint models with coarser grid spacings.

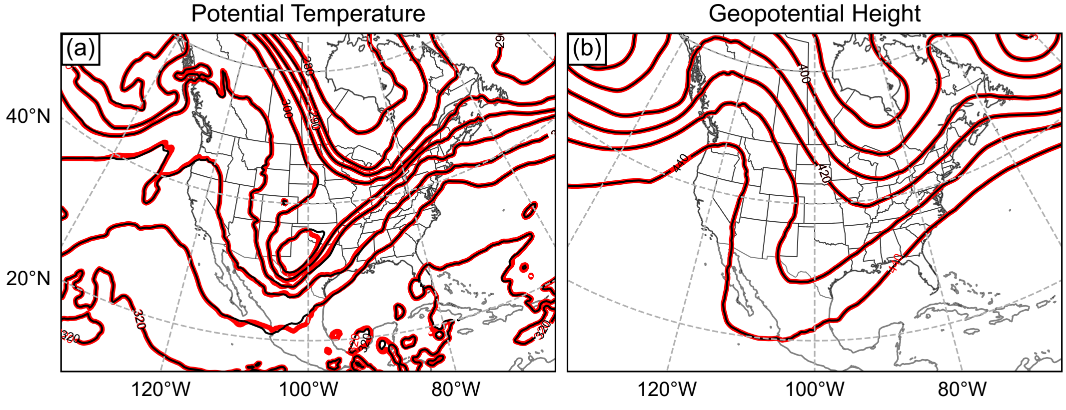

FIG. 5. GFS analysis (black) and GFS analysis plus the adjoint-derived perturbations (red) at 1200 UTC 13 Nov 2018 for 600-hPa (a) potential temperature (contoured every 5 K) and (b) geopotential height (contoured every 10 dam).

Brought to you by NAVAL RESEARCH LABORATORY | Unauthenticated | Downloaded 02/06/25 06:40 PM UTC

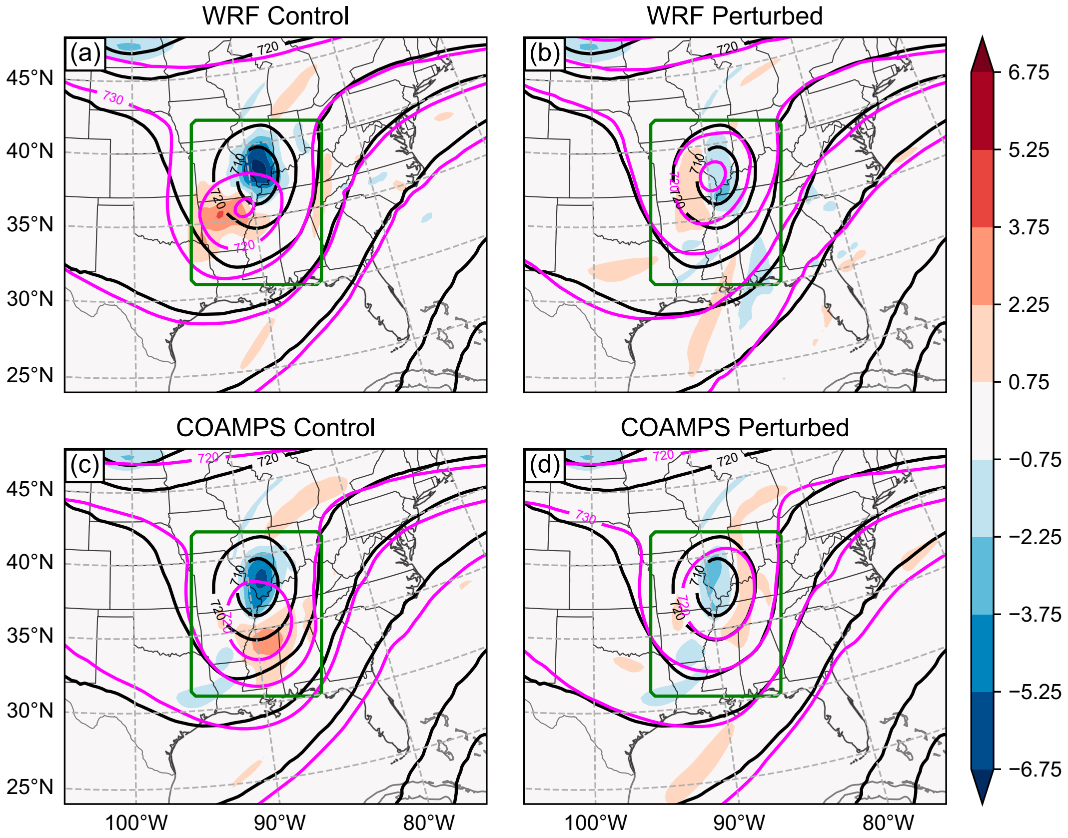

FIG. 6. 48-h errors (valid at 1200 UTC 15 Nov 2018) in the forecast of the upper-level cutoff low for the 30-km (a) control WRF, (b) adjoint-perturbed WRF, (c) control COAMPS, and (d) adjoint-perturbed COAMPS simulations. 400-hPa geopotential height is contoured every 10 dam for the GFS analysis (black) and the forecast (magenta). The forecast minus the GFS analysis for PV averaged between 300 and 500 hPa (color fill) is contoured every 1.5 PVU (1 PVU = 10^{-6} K kg^{-1} m^2 s^{-1}). The green contour bounds the response-function region used to compute the adjoint perturbations.

Rather than employing a convergence criterion, we iterate n times until we qualitatively determine that the solution is sufficiently close to the analysis. This results in the initial conditions $\mathbf{x}_0^{(n)}$ that yield the corrected forecast,

$$\mathbf{x}_0^{(n)} = \mathbf{x}_0 + \delta\mathbf{x}_0^{(1)} + \delta\mathbf{x}_0^{(2)} + \cdots + \delta\mathbf{x}_0^{(n)}, \qquad (7)$$

and the optimal perturbations that produce this correction are $\delta\mathbf{x}_0 = \mathbf{x}_0^{(n)} - \mathbf{x}_0$. Note that the scaling parameter s from (4) is imposed on the initial-condition perturbations at each iteration, so the maximum accumulated perturbation is allowed to exceed unity. We use $n = 9$ iterations to produce a forecast that is sufficiently close to the analysis. Appendix B includes details on our choice of n and a discussion of how the structure and amplitude of the perturbations change between iterations.

4. Simulations with parameterized convection

a. *Structure and impact of the perturbations*

To illustrate the structure of the adjoint-derived perturbations that correct the forecast bust, Fig. 4 depicts the square root of their difference total energy (DTE; Zhang et al. 2007), which is given by

$$\mathrm{DTE} = \frac{1}{2}\left[(\delta u)^2 + (\delta v)^2 + \frac{c_p}{T_r}(\delta T)^2\right], \qquad (8)$$

where δu, δv, and δT are the zonal-wind, meridional-wind, and temperature perturbations, respectively; $c_p = 1004$ J K^{-1} kg^{-1} is the specific heat at constant pressure; and $T_r = 270$ K is the reference temperature.

The perturbations are widespread in both the horizontal and the vertical, indicating that the forecast for the upper-level cutoff low is sensitive to the initial conditions along the entire longwave ridge–trough pattern throughout the troposphere. The areas of strongest sensitivity are generally associated with the trough in the lower and middle troposphere but extend over a large region from the Gulf of Mexico at 850 hPa (Fig. 4f) to the Great Plains at 600 and 700 hPa (Figs. 4d,e) to west-central Mexico at 500 hPa (Fig. 4c). There is also substantial amplitude associated with the upstream ridge over the western United States and western Canada, especially in the upper troposphere (Figs. 4a,b).

Brought to you by NAVAL RESEARCH LABORATORY | Unauthenticated | Downloaded 02/06/25 06:40 PM UTC

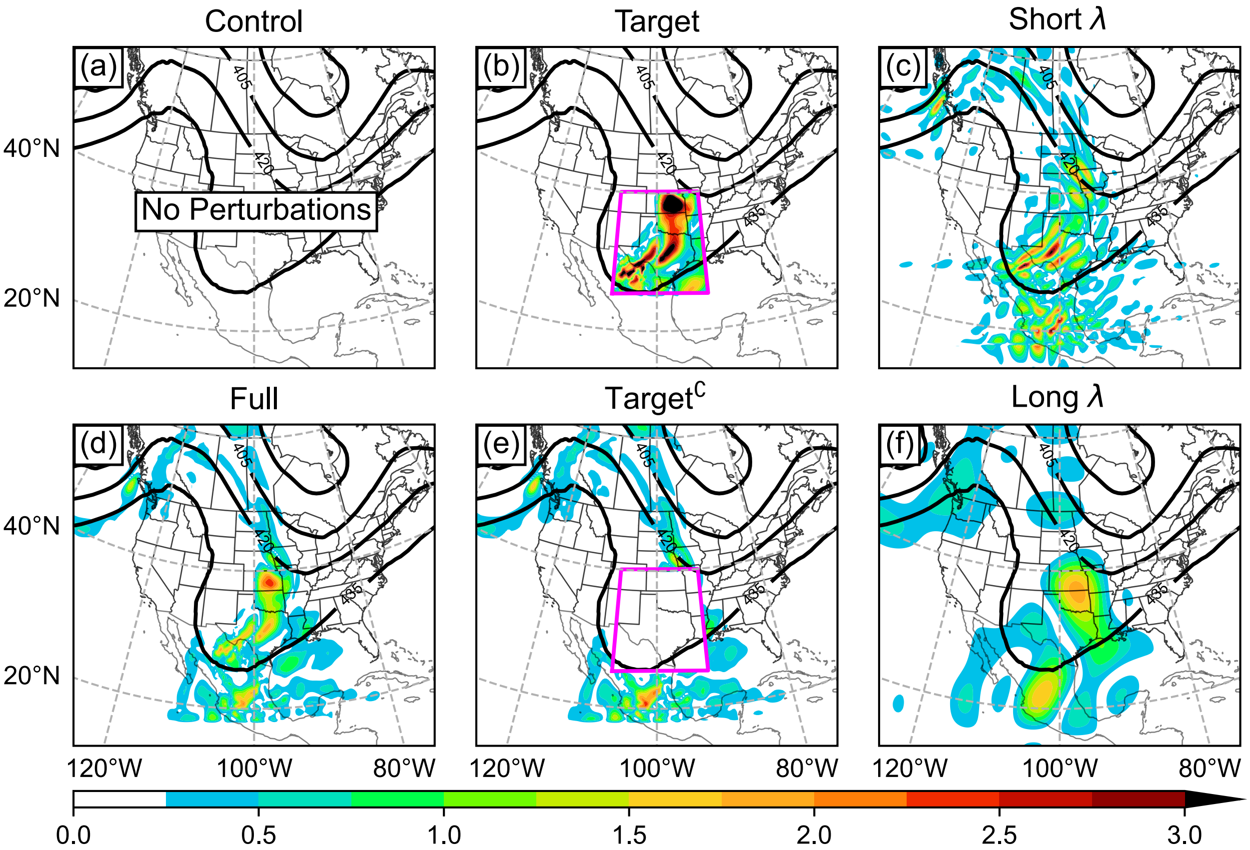

FIG. 7. Square root of the DTE of the perturbations (color fill every 0.25 m s^{-1}) at 600 hPa for the (b) target, (c) short-λ, (d) full, (e) target^C, and (f) long-λ experiments. The GFS analysis for 600-hPa geopotential height at 1200 UTC 13 Nov 2018 is contoured in black every 15 dam. The magenta contours in (b) and (e) bound the target region.

The perturbations are widespread and have maximum absolute values of 2.2 K for temperature and 1.2 m s^{-1} for horizontal wind speed, but they are too small in amplitude throughout most of the domain to make noticeable synoptic-scale changes to the initial conditions, as shown in Fig. 5. The only apparent differences between the perturbed and unperturbed 600-hPa potential-temperature fields are slight kinks in the contours over Mexico and the southern Great Plains (Fig. 5a). The differences are even less evident when looking at the 600-hPa geopotential height fields (Fig. 5b). These plots highlight a fundamental challenge of midlatitude-cyclone predictability: the initial-state differences between a poor forecast and a much better one can be large in scale yet so small in amplitude that they do not make distinguishable changes to the key synoptic-scale features at the initial time that drive the cyclone's development.

The 48-h forecast corrections produced by the adjoint-derived perturbations are shown in Fig. 6. In the 30-km control WRF forecast with unperturbed initial conditions, the cutoff low is well southwest of the analysis and the average squared PV error in the response-function region is 3.6 PVU^2 (Fig. 6a). When the adjoint-derived perturbations from COAMPS are interpolated onto the WRF grid and added to the initial conditions, the forecast for the cutoff low is in nearly the same location as the analysis, and the average squared PV error in the response-function region is reduced to 0.82 PVU^2 (Fig. 6b). Notably, the perturbations are effective at improving the 30-km WRF forecast despite being computed using the COAMPS adjoint. The control nonlinear COAMPS forecast is slightly more accurate than WRF, with a cutoff low that is also too far south but is more in phase with the analysis (Fig. 6c). Yet the perturbations improve the COAMPS forecast similarly to WRF, moving the cutoff low closer to the analysis and reducing the average squared PV error in the response-function region from 2.4 to 0.74 PVU^2 (Fig. 6d). These results indicate that it is reasonable to use the perturbations from the COAMPS adjoint in experiments with WRF. They also suggest that the initial-condition sensitivities are robust and not strongly dependent on the model used.

b. *Experiments with modified perturbations*

The sensitivity pattern for this forecast bust is generally widespread and large in scale, but the highest-amplitude structures are localized and smaller in scale (e.g., the feature over Kansas at 600 hPa in Fig. 4d). Thus, a relevant question from a targeting perspective is whether making the requisite

Brought to you by NAVAL RESEARCH LABORATORY | Unauthenticated | Downloaded 02/06/25 06:40 PM UTC

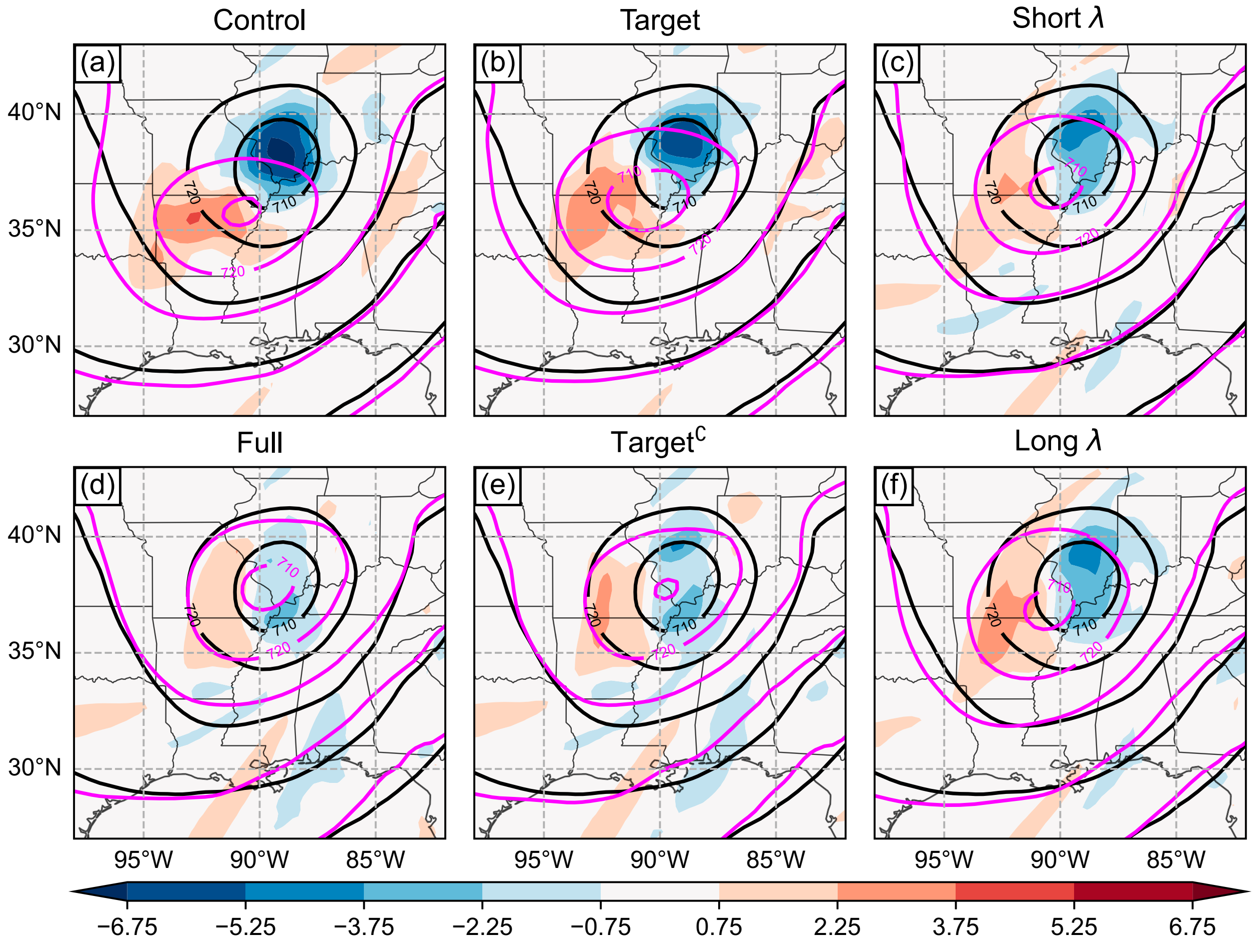

FIG. 8. 48-h errors (valid at 1200 UTC 15 Nov 2018) in the 30-km WRF forecast of the upper-level cutoff low for the (a) control, (b) target, (c) short-λ, (d) full, (e) target$^{\complement}$, and (f) long-λ experiments. 400-hPa geopotential height is contoured every 10 dam for the GFS analysis (black) and the WRF forecast (magenta). The WRF forecast minus the GFS analysis for PV averaged between 300 and 500 hPa (color fill) is contoured every 1.5 PVU.

changes to the initial conditions only in localized, small-scale regions still produces substantial improvement to the forecast. To test this, we run a series of 30-km WRF simulations in which the adjoint-derived perturbations are modified to retain only a specific component of the perturbation field.

Figure 7 shows the square root of the DTE at 600 hPa for each of the experiments. The WRF simulation with unperturbed initial conditions is the "control" experiment (Fig. 7a). The "full" experiment (Fig. 7d) corresponds to the WRF simulation in which the full, unmodified adjoint perturbations are added to the initial conditions. For the "target" experiment (Fig. 7b), the perturbations are confined to a 15° × 15° region, which is a typical size for aircraft targeting missions (e.g., Majumdar et al. 2002b, their Fig. 2). The placement of this region is somewhat subjective, but a sensible choice is over northern Mexico and the southern Great Plains because it includes the high-DTE features at 700 and 600 hPa while also including perturbations with substantial amplitude at 500, 400, and 300 hPa (see the magenta contours in Fig. 4). In set theory, the complement of a set A, denoted by $A^{\complement}$, is the set of elements not in A. Thus, the "target$^{\complement}$" experiment (Fig. 7e) involves setting the perturbations within the target region to zero and retaining the rest. To address the issue of scale dependence, we truncate the perturbations in spectral space to filter the perturbations by wavelength λ. For the "short-λ" experiment (Fig. 7c), only wavelengths shorter than 1000 km are retained, and for the "long-λ" experiment (Fig. 7f), only wavelengths longer than 1000 km are retained.

Since removing different components of the perturbations reduces their amplitudes to different degrees, we rescale each set of modified perturbations so that their domain-integrated DTE equals that of the full adjoint perturbations. This rescaling causes the target and short-λ perturbations to be greater in the maximum amplitude than the target$^{\complement}$ and long-λ perturbations, and it runs the risk of overcorrecting certain aspects of the forecast, but it nevertheless allows for the most equitable comparison between the impacts of the different perturbations.

Brought to you by NAVAL RESEARCH LABORATORY | Unauthenticated | Downloaded 02/06/25 06:40 PM UTC

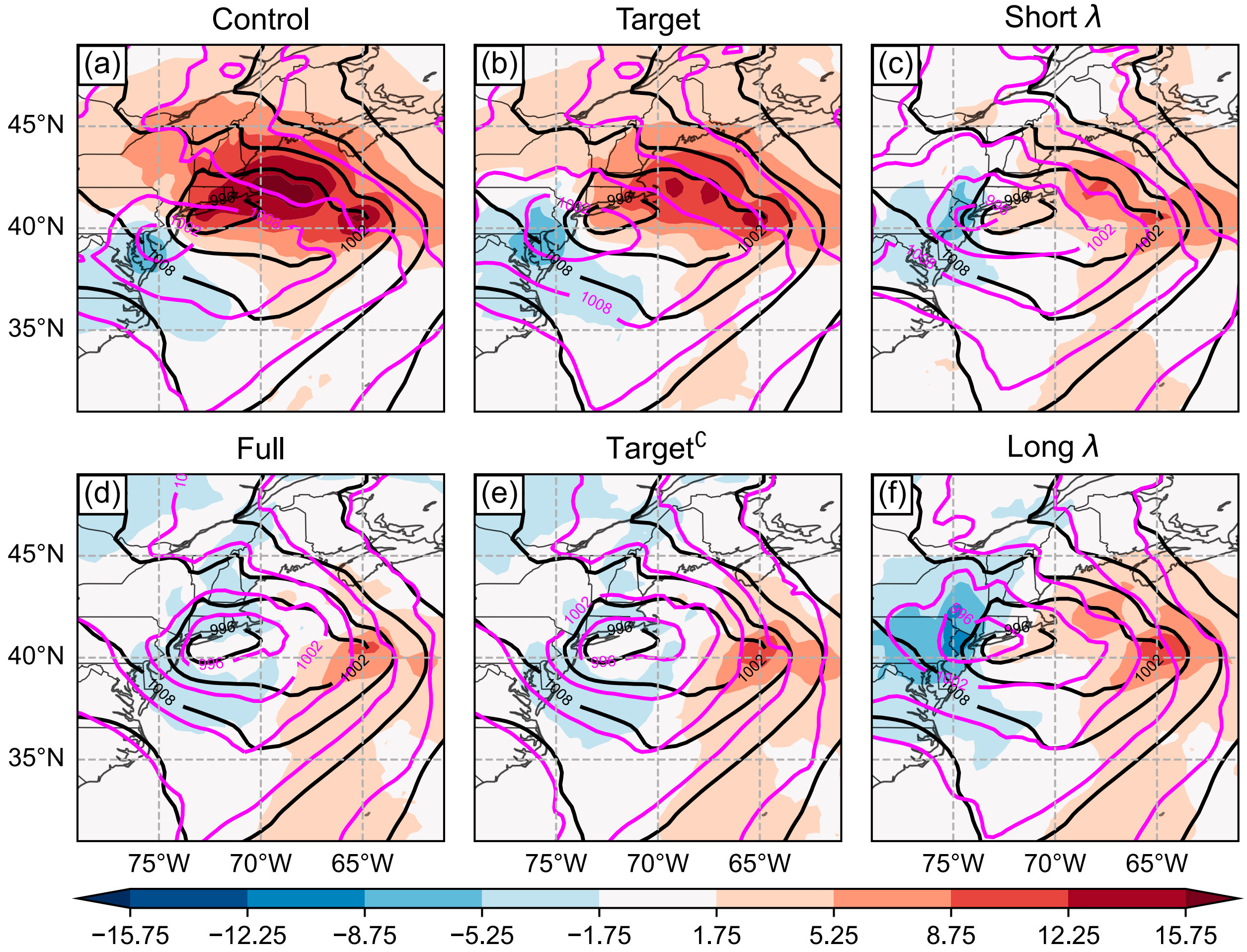

FIG. 9. 72-h errors (valid at 1200 UTC 16 Nov 2018) in the 30-km WRF forecast of the surface cyclone for the (a) control, (b) target, (c) short-λ, (d) full, (e) target^C, and (f) long-λ experiments. Sea level pressure is contoured every 6 hPa for the GFS analysis (black) and the WRF forecast (magenta). The WRF forecast minus the GFS analysis for sea level pressure (color fill) is contoured every 3.5 hPa.

Figure 8 shows the impacts of the different perturbations on the 48-h, 30-km WRF forecast for the upper-level cutoff low. In the target experiment (Fig. 8b), the localized perturbations do produce a cutoff low that is closer to the analysis in both location and intensity than the unperturbed control simulation (cf. Fig. 8a). Nevertheless, these improvements pale in comparison with those of the full adjoint perturbations (cf. Fig. 8d), as the cutoff low in the target experiment is still well southwest of the analysis and there remain substantial PV errors. The target^C perturbations (Fig. 8e) improve the forecast for the cutoff low considerably more than the target perturbations, particularly in terms of location. In fact, the target^C experiment has only slightly greater PV errors than the full experiment. Interestingly, both the short-λ (Fig. 8c) and long-λ (Fig. 8f) perturbations produce similar substantial improvements to the 48-h forecast, although neither match the improvement attained by the full or target^C perturbations.

Figure 9 shows that the 48-h forecast accuracy for the upper-level cutoff low at 1200 UTC 15 November 2018 is strongly associated with the 72-h forecast accuracy for the surface cyclone at 1200 UTC 16 November 2018. The control WRF forecast at 72 h (Fig. 9a) has the low over southern New Jersey with a minimum central pressure of about 1001 hPa, whereas the analysis has the low near Long Island with a minimum central pressure of about 995 hPa, amounting to errors in sea level pressure of about 15 hPa. These characteristics are similar to the 72-h GFS forecast for sea level pressure (Fig. 2b). The full adjoint perturbations (Fig. 9d) considerably improve the forecast for both the location and intensity of the surface cyclone. This is noteworthy because the perturbations are only optimized to reduce the forecast errors in the upper-level PV field at 48 h, yet they also substantially improve the 72-h forecast for the surface cyclone. This suggests that the upper-level cutoff low was a key synoptic-scale forecast challenge associated with this bust.

The relative performances of the simulations with modified adjoint perturbations are similar in their 72-h surface forecasts as in their 48-h upper-level forecasts. The target^C perturbations (Fig. 9e) produce substantial reductions in both location and intensity errors for the surface cyclone that are comparable to

Brought to you by NAVAL RESEARCH LABORATORY | Unauthenticated | Downloaded 02/06/25 06:40 PM UTC

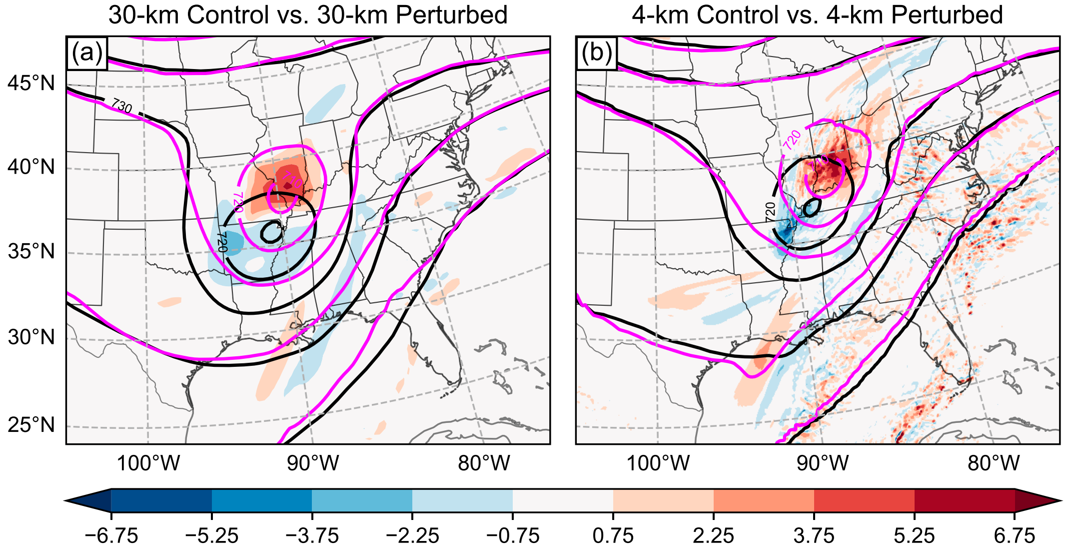

FIG. 10. 48-h differences (valid at 1200 UTC 15 Nov 2018) between the control and adjoint-perturbed forecasts for the upper-level cutoff low for the (a) 30- and (b) 4-km WRF simulations. 400-hPa geopotential height is contoured every 10 dam for the control (black) and perturbed (magenta) forecasts. The perturbed forecast minus the control forecast for PV averaged between 300 and 500 hPa (color fill) is contoured every 1.5 PVU.

those of the full adjoint perturbations, whereas the target experiment (Fig. 9b) performs nearly as poorly as the unperturbed control simulation. Both the short-λ (Fig. 9c) and long-λ (Fig. 9f) perturbations yield substantial improvements to the 72-h surface-cyclone forecast, but neither match the improvements attained by the full or target^C perturbations.

Overall, the results of these WRF simulations with parameterized convection indicate that the widespread, smaller-amplitude components of the adjoint perturbations are most important for yielding substantial reductions in forecast error: confining the perturbations to the chosen localized target region of the strongest sensitivity substantially impedes their ability to improve the forecast, whereas eliminating the perturbations in that target region or over a range of wavelengths does not.

5. Simulations with explicit convection

The moist adjoint model is run with parameterized convection and 30-km grid spacing in order to satisfy the tangent-linear approximation, mitigate nonlinear instabilities, and avoid spurious sensitivities. Nevertheless, there has been considerable debate over the importance of moist convection to midlatitude-cyclone predictability, with some studies suggesting that the upscale growth of localized, small-scale initial-condition errors via convection plays a predominant role in forecast busts (Zhang et al. 2002; Rodwell et al. 2013) and others arguing that such upscale growth is overwhelmed by relatively small-amplitude initial-condition errors on much larger scales (Langland et al. 2002; Durran et al. 2013; Lloveras et al. 2023). The question thus emerges whether localized or small-scale perturbations are more impactful when upscale growth from moist convection is explicitly represented.

A challenge with addressing this question is that the 4-km WRF forecast differs substantially from the 30-km COAMPS run used to compute the adjoint perturbations. Whereas both the unperturbed 30-km WRF and COAMPS forecasts for the upper-level cutoff low are too far south of the analysis (Figs. 6a,c), the 4-km WRF simulation has the low further to the northeast (contrast the black contours in Fig. 10a with those in Fig. 10b). As a result, the forecast-error response function J in the 4-km WRF run is different from J in the 30-km COAMPS run that the perturbations are designed to minimize. So, when the perturbations are interpolated onto the 4-km WRF mesh and added to the initial conditions for the convection-permitting simulation, they do not improve the forecast accuracy.

Nevertheless, the perturbations still have a substantial impact on the forecast relative to the unperturbed control simulation. Figure 10 shows that the perturbations in the 4-km WRF run move the cutoff low to the northeast nearly as much as in the 30-km case, producing a similar pattern in the difference PV field. Thus, the perturbations clearly correspond to regions of strong initial-condition sensitivity for the 4-km run, even though they do not produce the forecast improvements they were optimized to make in the 30-km run. This suggests that the adjoint-derived perturbations are still useful for investigating the initial-condition sensitivity in our simulations with explicit convection, so long as we focus on forecast changes relative to the unperturbed control simulation rather than on forecast performance relative to the analysis.

To investigate whether the impacts of localized, small-scale perturbations are greater when moist convection is explicitly represented, we run 4-km WRF simulations with the same set of perturbations as in the 30-km experiments (Fig. 7) but interpolated onto the 4-km mesh. Figure 11 shows the impacts of these perturbations on the 48-h forecast of the upper-level

Brought to you by NAVAL RESEARCH LABORATORY | Unauthenticated | Downloaded 02/06/25 06:40 PM UTC

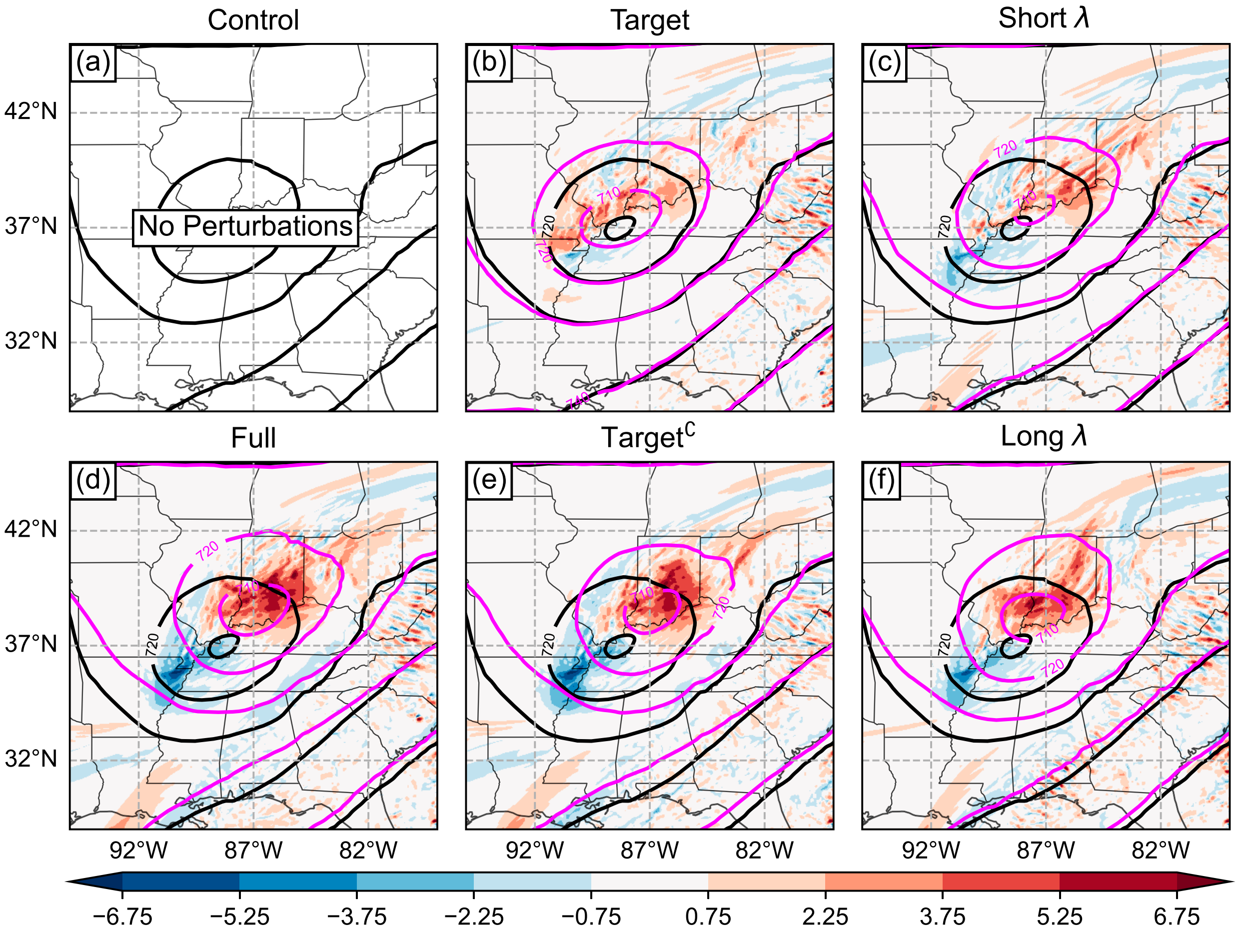

FIG. 11. 48-h changes (valid at 1200 UTC 15 Nov 2018) to the 4-km control WRF forecast of the upper-level cutoff low produced by the (b) target, (c) short-λ, (d) full, (e) target^{C}, and (f) long-λ perturbations. The 400-hPa geopotential height is contoured every 10 dam for the control (black) and perturbed (magenta) simulations. The perturbed run minus the control run for PV averaged between 300 and 500 hPa (color fill) is contoured every 1.5 PVU.

cutoff low. Note that in these plots, the more impactful perturbations exhibit more intense colors because they produce greater differences relative to the control simulation. This is in contrast to our presentation of the 30-km results (e.g., Fig. 8) in which the more impactful perturbations exhibit less intense colors because they produce solutions that are closer to the analysis.

Figures 11d and 11e show that the full and target^{C} perturbations have the strongest impacts on the 48-h forecast of the upper-level cutoff low, consistent with the 30-km experiments. Both of these perturbations deepen the cutoff low and move it more than 100 km to the northeast of the control. In contrast, the target perturbations (Fig. 11b) only deepen the low slightly and do not introduce noticeable differences in location. Interestingly, the long-λ perturbations (Fig. 11f) cause greater changes than the short-λ perturbations (Fig. 11c) to both the intensity and location of the cutoff low in the 4-km simulations, whereas they are about equally impactful in the 30-km runs (cf. Figs. 8c,f).

Figure 12 shows that the perturbations that cause the greatest changes to the upper-level cutoff low at 48 h cause the greatest changes to the surface cyclone at 72 h, consistent with the 30-km experiments. The full and target^{C} perturbations (Figs. 12d,e) produce nearly identical changes to the surface cyclone, moving the low-pressure center several hundred kilometers to the northeast and resulting in differences in sea level pressure of nearly 15 hPa. In contrast, the target perturbations produce only a very minor northeastward shift in the cyclone's location (Fig. 12b). The short- and long-λ perturbations (Figs. 12c,f) produce similar shifts to those in the full and target^{C} experiments, but as for the 48-h forecast of the cutoff low, the long-λ perturbations have a greater impact on the surface cyclone at 72 h than the short-λ perturbations.

To provide a quantitative, overall assessment of the impact of each set of perturbations on the simulations with explicit convection, Fig. 13 depicts the 72-h evolution of domain-integrated DTE. Recall that we configure the sets of perturbations to be equal in initial domain-integrated DTE. The time series shows that the greatest differences at 48–72-h lead times are produced by the perturbations that are widespread or large in scale (solid curves) rather than by the

Brought to you by NAVAL RESEARCH LABORATORY | Unauthenticated | Downloaded 02/06/25 06:40 PM UTC

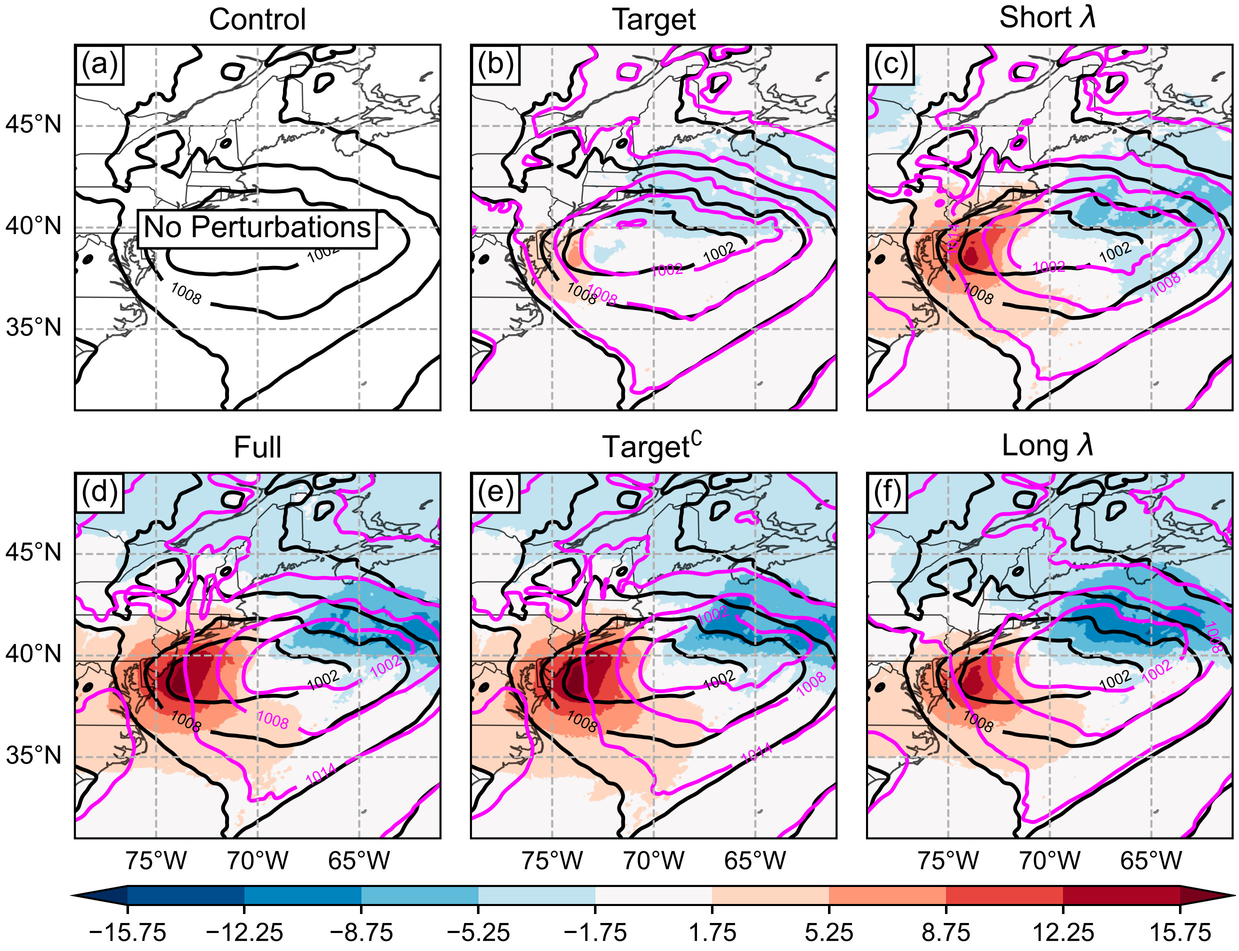

FIG. 12. 72-h changes (valid at 1200 UTC 16 Nov 2018) to the 4-km control WRF forecast of the surface cyclone produced by the (b) target, (c) short-λ, (d) full, (e) target^{C}, and (f) long-λ perturbations. Sea level pressure is contoured every 6 hPa for the control (black) and perturbed (magenta) simulations. The perturbed run minus the control run for sea level pressure (color fill) is contoured every 3.5 hPa.

perturbations that are localized or small in scale (dashed curves). The full and target^{C} experiments have the greatest DTE, and the target experiment has the least throughout the integration period. The short- and long-λ experiments have similar DTE through 30 h, but the long-λ clearly has greater DTE at 48 h, and this separation becomes even more apparent by 72 h.

In summary, the explicit representation of convection does not enhance the impact of localized and small-scale perturbations relative to the smaller-amplitude but widespread and large-scale components of the sensitivity pattern. In fact, the long-λ perturbations have greater impacts than the short-λ perturbations in the 4-km simulations, whereas their impacts are about the same in the 30-km runs.

6. Conclusions

A potential contributing factor to the often-underwhelming results from targeted observations for midlatitude cyclones is that the benefits of reducing initial-condition errors over a localized sensitive region can be overwhelmed by smaller-amplitude but widespread sensitivities outside of that region. In this paper, we test this hypothesis on a forecast bust for a midlatitude cyclone that impacted the East Coast of the United States on 15 November 2018. We use iterative runs of a moist adjoint model to obtain the initial-condition perturbations that minimize the 48-h forecast errors associated with the cyclone's precursor upper-level cutoff low. When added to the initial conditions for WRF simulations with parameterized convection, the adjoint-optimal perturbations substantially improve the location and intensity forecasts both for the upper-level cutoff low at a 48-h lead time and for the surface cyclone at a 72-h lead time. These perturbations extend throughout the troposphere and over a longwave ridge–trough pattern covering much of North America. Although the local-maximum perturbations have absolute values of 2.2 K for temperature and 1.2 m s^{-1} for horizontal wind speed, the changes they produce on maps of potential temperature and geopotential height are almost invisible.

To test our hypothesis about targeting, we run a series of WRF simulations with parameterized convection in which the

Brought to you by NAVAL RESEARCH LABORATORY | Unauthenticated | Downloaded 02/06/25 06:40 PM UTC

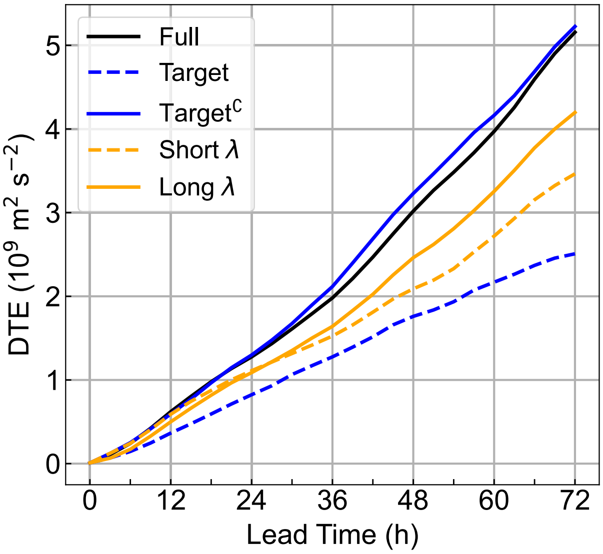

FIG. 13. Time series of domain-integrated DTE through 72 h of lead time for the initial-condition-perturbation experiments with explicit convection.

perturbations are modified to retain only a specific component of the perturbation field and are rescaled to be equal in a domain-integrated energy norm to the full, unmodified perturbations. When the perturbations are confined to a 15° × 15° target region of the strongest sensitivity, they do not produce substantial improvements to the forecast. In contrast, when the perturbations within this target region are removed and the rest of the perturbations (which are smaller in maximum amplitude but are much more widespread) are retained, they yield substantial forecast improvements comparable to those produced by the full adjoint-optimal perturbations. When the perturbations are filtered to retain only wavelengths shorter than 1000 km, they produce similar considerable forecast improvements as when only wavelengths longer than 1000 km are retained. However, neither the short- nor the long-wavelength perturbations improve the forecast as much as the full perturbations or those with only the target region removed.

Since the 30-km simulations do not explicitly represent the potentially rapid growth of small-scale, localized initial-condition errors from moist convection, we also evolve the perturbations in convection-permitting 4-km WRF runs. The forecast errors in the convection-permitting run differ from those in the coarser-resolution simulation used to run the adjoint model, so the perturbations do not lead to a correction of the forecast. Nevertheless, the perturbations have a substantial impact on the convection-permitting forecast relative to the unperturbed control simulation, so they are still useful for investigating the initial-condition sensitivity of the high-resolution forecast. Thus, for the simulations with explicit convection, we focus on how the perturbations change the forecast relative to the control run, rather than on how they impact forecast accuracy. When the perturbations are confined to the chosen 15° × 15° target region, they are less impactful than when the perturbations inside the target region are removed and the rest of the perturbations are retained. This result is consistent with the coarser-resolution experiments with parameterized convection. Interestingly, however, the long-wavelength perturbations are more impactful than the short-wavelength ones in the convection-permitting runs, whereas they are about equally as impactful in the runs with parameterized convection.

These results support our hypothesis that improving the initial conditions over a localized target region may not mitigate a midlatitude-cyclone forecast bust if smaller-amplitude but widespread sensitivities outside of the target region are not adequately constrained by the observational network. Indeed, the most impactful initial-condition differences between an accurate forecast and a poor one can be widespread, yet so small in amplitude that they do not make distinguishable adjustments to the synoptic features at the initial time that drive the cyclone's development. In these cases, improving the analysis over a broad region (e.g., by improving the coverage and assimilation of satellite observations) may be more fruitful in preventing a forecast bust than deploying targeted rawinsondes or aircraft observations to a particular sensitive area.

The adjoint technique provides diagnostic insight into initial-condition changes that could have prevented the forecast bust, but a limitation is that it does not take into account the likelihood that the sensitivity patterns represent actual errors in the analysis (Isaksen et al. 2005). The degree of improvement from targeted observations depends not only on the initial-condition sensitivity but also on the routinely available observations and the data assimilation system. Another limitation of the adjoint method is that it does not consider the influence of model error. However, the fact that the GFS, WRF, and COAMPS models exhibit similar errors and the adjoint-derived perturbations from COAMPS evolve similarly in both COAMPS and WRF suggests that initial-condition errors were more important for this forecast bust than model errors.

Our study is also limited to a single midlatitude-cyclone bust case. Poor forecasts of events like the 15 November 2018 East Coast cyclone that are associated with highly amplified longwave ridge–trough patterns may be particularly difficult to address with targeted observations. Even so, our results are consistent with targeting efforts for mesoscale convective systems from the Mesoscale Predictability Experiment (MPEX; Weisman et al. 2015). While the sensitive regions for mesoscale convective systems can be small in scale and localized to important dynamical features (Hill et al. 2016), Romine et al. (2016) showed that sampling both the disturbance and the surrounding environment is essential to getting forecast improvements from targeted observations. Sampling both the disturbance and the adjacent flow with targeted observations may not be practical for synoptic-scale systems like the 15 November 2018 East Coast cyclone, but it can be more feasible for smaller-scale phenomena. This may explain why targeted observations can be more beneficial for mesoscale convective systems (Hill et al. 2021), tropical cyclones (Sippel et al. 2022), and atmospheric rivers (Lord et al. 2022).

Brought to you by NAVAL RESEARCH LABORATORY | Unauthenticated | Downloaded 02/06/25 06:40 PM UTC

Acknowledgments. Daniel J. Lloveras and Dale R. Durran acknowledge the support of Grant N00014-20-1-2387 from the Office of Naval Research. Daniel J. Lloveras was partly supported by an appointment to the National Research Council (NRC) Research Associateship Program at the Naval Research Laboratory, administered by the Fellowships Office of the National Academies of Sciences, Engineering, and Medicine. James D. Doyle acknowledges the support of the Naval Research Laboratory Base Program through Program Element 0601153N. We acknowledge the computational resources from the Navy Department of Defense Supercomputing Resource Center in Stennis, Mississippi. We are grateful for constructive reviews from Aaron Hill and three anonymous reviewers.

Data availability statement. The GFS data are publicly available at https://rda.ucar.edu/datasets/ds084.1, and the GEFS data are publicly available at https://noaa-gefs-pds.s3.amazonaws.com/index.html. The WRF and COAMPS output files used in this study are too large to publicly archive or to transfer. However, the control simulations can be easily reproduced because the GFS data used for the initial and boundary conditions are publicly available, and the WRF Model is publicly available at https://github.com/wrf-model/WRF/releases/tag/v4.4. The perturbed simulations can be reproduced by adding the adjoint perturbations to the initial conditions, which are archived with the University of Washington Libraries ResearchWorks repository at https://hdl.handle.net/1773/51016.

APPENDIX A

Robustness of the Forecast Bust

Was the 15 November 2018 forecast bust limited to deterministic runs initialized from the GFS analysis? To address this, Fig. A1 shows the forecasts from the Global Ensemble Forecast System (GEFS) for the upper-level cutoff low and the ensuing surface cyclone. All 21 ensemble members had the upper-level cutoff low and the surface cyclone too far southwest of the analysis, indicating that the forecast uncertainty for this event was not adequately represented by the GEFS. This can be interpreted as another type of forecast bust. Also, Fig. A2 shows that the Navy Global Environmental Model (NAVGEM; Hogan et al. 2014) forecast had the cutoff low and surface cyclone in similar spots to the GFS forecast, indicating that the bust was not limited to simulations with initial conditions from GFS analysis.

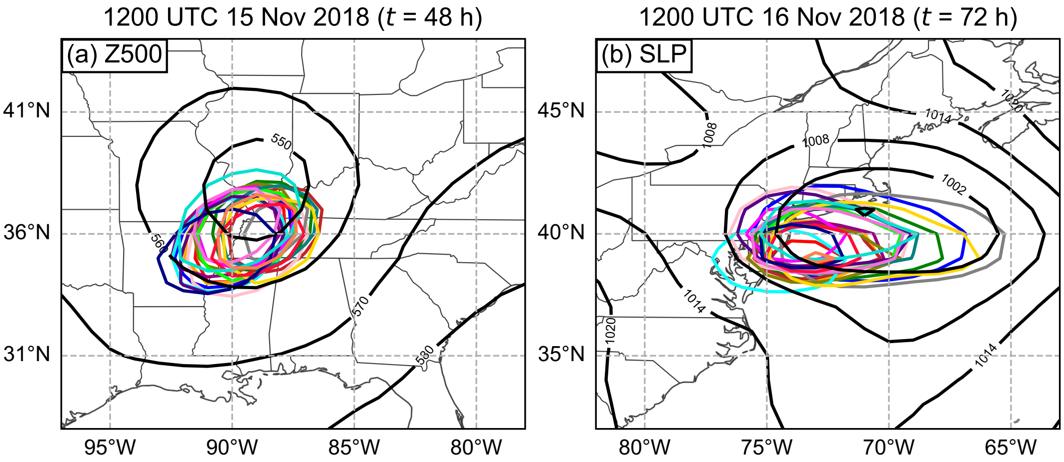

FIG. A1. (a) 48-h forecasts for 500-hPa geopotential height (Z500) and (b) 72-h forecasts for sea level pressure (SLP) for the 21 members of the GEFS initialized at 1200 UTC 13 Nov 2018. Colors indicate the 550-dam (Z500) and 1002-hPa (SLP) contours for each ensemble member. The GFS analysis is contoured in black every 10 dam for Z500 and every 6 hPa for SLP.

Brought to you by NAVAL RESEARCH LABORATORY | Unauthenticated | Downloaded 02/06/25 06:40 PM UTC

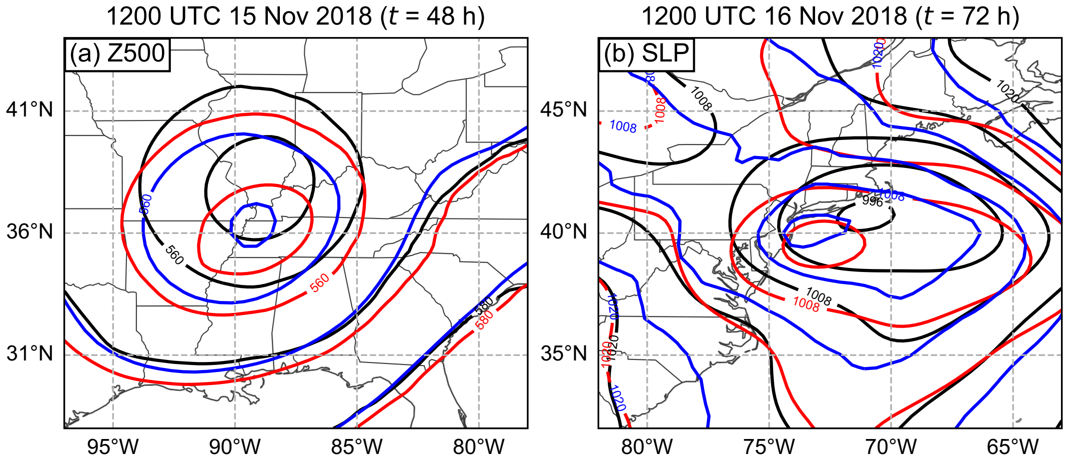

FIG. A2. (a) 48-h forecasts for 500-hPa geopotential height (Z500) and (b) 72-h forecasts for sea level pressure (SLP) for the GFS (red) and NAVGEM (blue) runs initialized at 1200 UTC 13 Nov 2018. The GFS analysis is in black. Contours are every 10 dam for Z500 and every 6 hPa for SLP.

APPENDIX B

Details of the Iterative Adjoint Procedure

An advantage of the ad hoc iterative procedure described in section 3c is that it allows for the examination of the perturbations (to see if they are reasonable in structure and amplitude) and their impact (to see if the forecast improvement is qualitatively sufficient) at each iteration. This allows for the procedure to be stopped if an iteration has introduced unrealistic noise to the perturbations (Klinker et al. 1998), and it allows for the procedure to be continued if more improvements to the forecast are desired. The appropriate number of iterations depends on the case and on the method used to scale the perturbations at each iteration. For example, Langland et al. (2002) used only two iterations to correct their forecast of the 25 January 2000 snowstorm, whereas Kleist and Morgan (2005) corrected their forecast of the same storm with 12 iterations, using a very small scaling factor at each

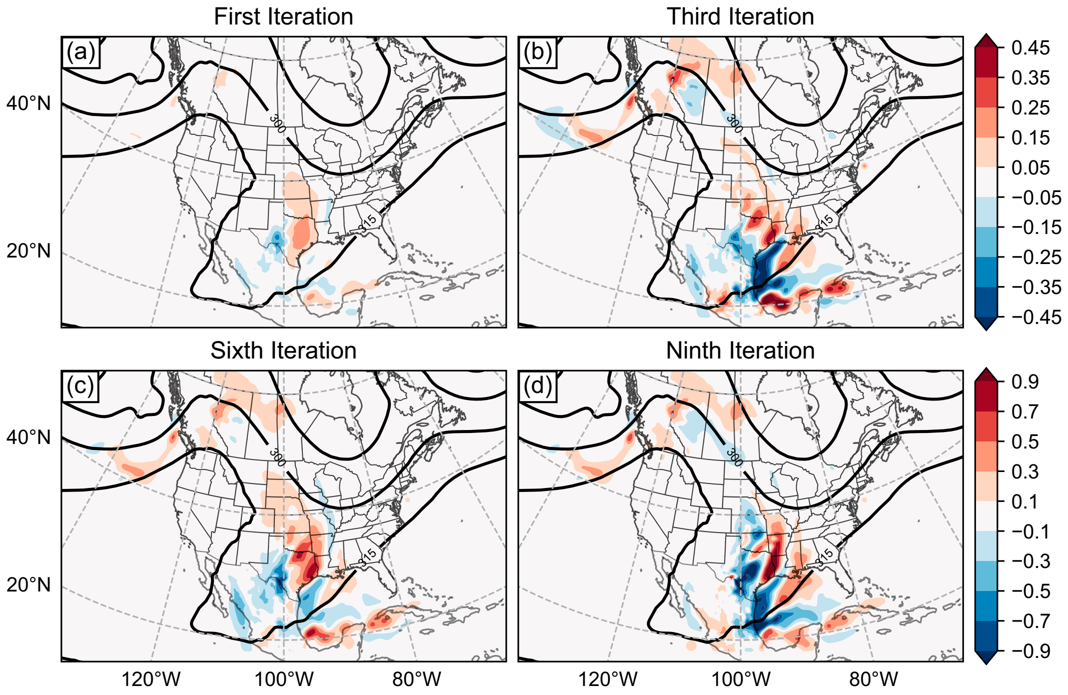

FIG. B1. 700-hPa adjoint-derived potential-temperature perturbations at the (a) first, (b) third, (c) sixth, and (d) ninth iterations, color filled every 0.1 K for the first and third iterations and every 0.2 K for the sixth and ninth iterations. The GFS analysis for 700-hPa geopotential height is contoured in black every 15 dam.

Brought to you by NAVAL RESEARCH LABORATORY | Unauthenticated | Downloaded 02/06/25 06:40 PM UTC

iteration. In our study, we use nine iterations because they produce substantial forecast correction (Fig. 6) without introducing unrealistic noise to the perturbations (Figs. 4 and B1).

To demonstrate how the perturbations evolve through the iterations, Fig. B1 shows the 700-hPa potential-temperature perturbations after the first, third, sixth, and ninth iterations. The perturbations increase in amplitude at each iteration, with the maximum perturbation increasing from 0.3 K after the first iteration to 1.6 K after the ninth. The general locations of the strongest sensitivity do not change between iterations, as features over the western Gulf of Mexico, the southern Great Plains of the United States, and western Canada are apparent at each iteration. Nevertheless, the relative amplitudes and small-scale details of these features change between iterations. For example, the region with negative perturbations over the western Gulf of Mexico has the greatest amplitude after the third iteration, but after the sixth iteration, the region with positive perturbations over eastern Texas has the greatest amplitude.

REFERENCES

Amerault, C., X. Zou, and J. D. Doyle, 2008: Tests of an adjoint mesoscale model with explicit moist physics on the cloud scale. *Mon. Wea. Rev.*, **136**, 2120–2132, https://doi.org/10.1175/2007MWR2259.1.

Ancell, B., and G. J. Hakim, 2007: Comparing adjoint- and ensemble-sensitivity analysis with applications to observation targeting. *Mon. Wea. Rev.*, **135**, 4117–4134, https://doi.org/10.1175/2007MWR1904.1.

Bauer, P., A. Thorpe, and G. Brunet, 2015: The quiet revolution of numerical weather prediction. *Nature*, **525**, 47–55, https://doi.org/10.1038/nature14956.

Bishop, C. H., B. J. Etherton, and S. J. Majumdar, 2001: Adaptive sampling with the ensemble transform Kalman filter. Part I: Theoretical aspects. *Mon. Wea. Rev.*, **129**, 420–436, https://doi.org/10.1175/1520-0493(2001)129<0420:ASWTET>2.0.CO;2.

Doyle, J. D., C. Amerault, C. A. Reynolds, and P. A. Reinecke, 2014: Initial condition sensitivity and predictability of a severe extratropical cyclone using a moist adjoint. *Mon. Wea. Rev.*, **142**, 320–342, https://doi.org/10.1175/MWR-D-13-00201.1.

——, C. A. Reynolds, and C. Amerault, 2019: Adjoint sensitivity analysis of high-impact extratropical cyclones. *Mon. Wea. Rev.*, **147**, 4511–4532, https://doi.org/10.1175/MWR-D-19-0055.1.

Durran, D. R., P. A. Reinecke, and J. D. Doyle, 2013: Large-scale errors and mesoscale predictability in Pacific Northwest snowstorms. *J. Atmos. Sci.*, **70**, 1470–1487, https://doi.org/10.1175/JAS-D-12-0202.1.

Errico, R. M., 1997: What is an adjoint model? *Bull. Amer. Meteor. Soc.*, **78**, 2577–2592, https://doi.org/10.1175/1520-0477(1997)078<2577:WIAAM>2.0.CO;2.

Hamill, T. M., F. Yang, C. Cardinali, and S. J. Majumdar, 2013: Impact of targeted winter storm reconnaissance dropwindsonde data on midlatitude numerical weather predictions. *Mon. Wea. Rev.*, **141**, 2058–2065, https://doi.org/10.1175/MWR-D-12-00309.1.

Hill, A. J., C. C. Weiss, and B. C. Ancell, 2016: Ensemble sensitivity analysis for mesoscale forecasts of dryline convection initiation. *Mon. Wea. Rev.*, **144**, 4161–4182, https://doi.org/10.1175/MWR-D-15-0338.1.

——, ——, and D. C. Dowell, 2021: Influence of a portable near-surface observing network on experimental ensemble forecasts of deep convection hazards during VORTEX-SE. *Wea. Forecasting*, **36**, 1141–1167, https://doi.org/10.1175/WAF-D-20-0237.1.

Hodur, R. M., 1997: The Naval Research Laboratory's Coupled Ocean/Atmosphere Mesoscale Prediction System (COAMPS). *Mon. Wea. Rev.*, **125**, 1414–1430, https://doi.org/10.1175/1520-0493(1997)125<1414:TNRLSC>2.0.CO;2.

Hogan, T. F., and Coauthors, 2014: The Navy Global Environmental Model. *Oceanography*, **27** (3), 116–125, https://doi.org/10.5670/oceanog.2014.73.

Hoskins, B., 2013: The potential for skill across the range of the seamless weather-climate prediction problem: A stimulus for our science. *Quart. J. Roy. Meteor. Soc.*, **139**, 573–584, https://doi.org/10.1002/qj.1991.

Isaksen, L., M. Fisher, E. Andersson, and J. Barkmeijer, 2005: The structure and realism of sensitivity perturbations and their interpretation as 'Key Analysis Errors'. *Quart. J. Roy. Meteor. Soc.*, **131**, 3053–3078, https://doi.org/10.1256/qj.04.99.

Janjić, Z. I., 1994: The step-mountain eta coordinate model: Further developments of the convection, viscous sublayer, and turbulence closure schemes. *Mon. Wea. Rev.*, **122**, 927–945, https://doi.org/10.1175/1520-0493(1994)122<0927:TSMECM>2.0.CO;2.

Joly, A., and Coauthors, 1999: Overview of the field phase of the Fronts and Atlantic Storm-Track Experiment (FASTEX) project. *Quart. J. Roy. Meteor. Soc.*, **125**, 3131–3163, https://doi.org/10.1002/qj.49712556103.

Kleist, D. T., and M. C. Morgan, 2005: Application of adjoint-derived forecast sensitivities to the 24–25 January 2000 U.S. East Coast snowstorm. *Mon. Wea. Rev.*, **133**, 3148–3175, https://doi.org/10.1175/MWR3023.1.

Klemp, J. B., J. Dudhia, and A. D. Hassiotis, 2008: An upper gravity-wave absorbing layer for NWP applications. *Mon. Wea. Rev.*, **136**, 3987–4004, https://doi.org/10.1175/2008MWR2596.1.

Klinker, E., F. Rabier, and R. Gelaro, 1998: Estimation of key analysis errors using the adjoint technique. *Quart. J. Roy. Meteor. Soc.*, **124**, 1909–1933, https://doi.org/10.1002/qj.49712455007.

Langland, R. H., 2005: Issues in targeted observing. *Quart. J. Roy. Meteor. Soc.*, **131**, 3409–3425, https://doi.org/10.1256/qj.05.130.

——, and N. L. Baker, 2004: Estimation of observation impact using the NRL atmospheric variational data assimilation adjoint system. *Tellus*, **56A**, 189–201, https://doi.org/10.3402/tellusa.v56i3.14413.

——, R. Gelaro, G. D. Rohaly, and M. A. Shapiro, 1999a: Targeted observations in FASTEX: Adjoint-based targeting procedures and data impact experiments in IOP17 and IOP18. *Quart. J. Roy. Meteor. Soc.*, **125**, 3241–3270, https://doi.org/10.1002/qj.49712556107.

——, and Coauthors, 1999b: The North Pacific Experiment (NORPEX-98): Targeted observations for improved North American weather forecasts. *Bull. Amer. Meteor. Soc.*, **80**, 1363–1384, https://doi.org/10.1175/1520-0477(1999)080<1363:TNPENT>2.0.CO;2.

——, M. A. Shapiro, and R. Gelaro, 2002: Initial condition sensitivity and error growth in forecasts of the 25 January 2000 East Coast snowstorm. *Mon. Wea. Rev.*, **130**, 957–974, https://doi.org/10.1175/1520-0493(2002)130<0957:ICSAEG>2.0.CO;2.

Lloveras, D. J., D. R. Durran, and J. D. Doyle, 2023: The two- to four-day predictability of midlatitude cyclones: Don't sweat the small stuff. *J. Atmos. Sci.*, **80**, 2613–2633, https://doi.org/10.1175/JAS-D-22-0232.1.

Brought to you by NAVAL RESEARCH LABORATORY | Unauthenticated | Downloaded 02/06/25 06:40 PM UTC

Lord, S. J., X. Wu, V. Tallapragada, and F. M. Ralph, 2022: The impact of dropsonde data on the performance of the NCEP Global Forecast System during the 2020 atmospheric rivers observing campaign. Part I: Precipitation. *Wea. Forecasting*, **38**, 17–45, https://doi.org/10.1175/WAF-D-22-0036.1.

Louis, J.-F., 1979: A parametric model of vertical eddy fluxes in the atmosphere. *Bound.-Layer Meteor.*, **17**, 187–202, https://doi.org/10.1007/BF00117978.

Magnusson, L., 2017: Diagnostic methods for understanding the origin of forecast errors. *Quart. J. Roy. Meteor. Soc.*, **143**, 2129–2142, https://doi.org/10.1002/qj.3072.

——, J.-H. Chen, S.-J. Lin, L. Zhou, and X. Chen, 2019: Dependence on initial conditions versus model formulations for medium-range forecast error variations. *Quart. J. Roy. Meteor. Soc.*, **145**, 2085–2100, https://doi.org/10.1002/qj.3545.

Mahfouf, J.-F., 1999: Influence of physical processes on the tangent-linear approximation. *Tellus*, **51A**, 147–166, https://doi.org/10.3402/tellusa.v51i2.12312.

Majumdar, S. J., 2016: A review of targeted observations. *Bull. Amer. Meteor. Soc.*, **97**, 2287–2303, https://doi.org/10.1175/BAMS-D-14-00259.1.

——, C. H. Bishop, R. Buizza, and R. Gelaro, 2002a: A comparison of ensemble-transform Kalman-filter targeting guidance with ECMWF and NRL total-energy singular-vector guidance. *Quart. J. Roy. Meteor. Soc.*, **128**, 2527–2549, https://doi.org/10.1256/qj.01.214.

——, ——, B. J. Etherton, and Z. Toth, 2002b: Adaptive sampling with the ensemble transform Kalman filter. Part II: Field program implementation. *Mon. Wea. Rev.*, **130**, 1356–1369, https://doi.org/10.1175/1520-0493(2002)130<1356:ASWTET>2.0.CO;2.

Miller, J. E., 1946: Cyclogenesis in the Atlantic coastal region of the United States. *J. Meteor.*, **3**, 31–44, https://doi.org/10.1175/1520-0469(1946)003<0031:CITACR>2.0.CO;2.

Molinari, J., 1985: A general form of Kuo's cumulus parameterization. *Mon. Wea. Rev.*, **113**, 1411–1416, https://doi.org/10.1175/1520-0493(1985)113<1411:AGFOKC>2.0.CO;2.

Novak, D. R., and Coauthors, 2023: Innovations in winter storm forecasting and decision support services. *Bull. Amer. Meteor. Soc.*, **104**, E715–E735, https://doi.org/10.1175/BAMS-D-22-0065.1.

Palmer, T. N., R. Gelaro, J. Barkmeijer, and R. Buizza, 1998: Singular vectors, metrics, and adaptive observations. *J. Atmos. Sci.*, **55**, 633–653, https://doi.org/10.1175/1520-0469(1998)055%3C0633:SVMAAO%3E2.0.CO;2.

Peevey, T. R., J. M. English, L. Cucurull, H. Wang, and A. C. Kren, 2018: Improving winter storm forecasts with observing system simulation experiments (OSSEs). Part I: An idealized case study of three U.S. storms. *Mon. Wea. Rev.*, **146**, 1341–1366, https://doi.org/10.1175/MWR-D-17-0160.1.

Rodwell, M. J., and Coauthors, 2013: Characteristics of occasional poor medium-range weather forecasts for Europe. *Bull. Amer. Meteor. Soc.*, **94**, 1393–1405, https://doi.org/10.1175/BAMS-D-12-00099.1.

Romine, G. S., C. S. Schwartz, R. D. Torn, and M. L. Weisman, 2016: Impact of assimilating dropsonde observations from MPEX on ensemble forecasts of severe weather events. *Mon. Wea. Rev.*, **144**, 3799–3823, https://doi.org/10.1175/MWR-D-15-0407.1.

Rutledge, S. A., and P. Hobbs, 1983: The mesoscale and microscale structure and organization of clouds and precipitation in midlatitude cyclones. VIII: A model for the "seeder-feeder" process in warm-frontal rainbands. *J. Atmos. Sci.*, **40**, 1185–1206, https://doi.org/10.1175/1520-0469(1983)040<1185:TMAMSA>2.0.CO;2.

Schindler, M., M. Weissmann, A. Schäfler, and G. Radnoti, 2020: The impact of dropsonde and extra radiosonde observations during NAWDEX in autumn 2016. *Mon. Wea. Rev.*, **148**, 809–824, https://doi.org/10.1175/MWR-D-19-0126.1.

Sippel, J. A., X. Wu, S. D. Ditchek, V. Tallapragada, and D. T. Kleist, 2022: Impacts of assimilating additional reconnaissance data on operational GFS tropical cyclone forecasts. *Wea. Forecasting*, **37**, 1615–1639, https://doi.org/10.1175/WAF-D-22-0058.1.

Skamarock, W. C., and Coauthors, 2021: A description of the Advanced Research WRF version 4.3. NCAR Tech. Note NCAR/TN-556+STR, 145 pp., https://doi.org/10.5065/1dfh-6p97.

Tewari, M., and Coauthors, 2004: Implementation and verification of the unified Noah land surface model in the WRF model. *20th Conf. on Weather Analysis and Forecasting/16th Conf. on Numerical Weather Prediction*, Seattle, WA, Amer. Meteor Soc., 14.2a, https://ams.confex.com/ams/84Annual/webprogram/Paper69061.html.

Thompson, G., P. R. Field, R. M. Rasmussen, and W. D. Hall, 2008: Explicit forecasts of winter precipitation using an improved bulk microphysics scheme. Part II: Implementation of a new snow parameterization. *Mon. Wea. Rev.*, **136**, 5095–5115, https://doi.org/10.1175/2008MWR2387.1.

Tiedtke, M., 1989: A comprehensive mass flux scheme for cumulus parameterization in large-scale models. *Mon. Wea. Rev.*, **117**, 1779–1800, https://doi.org/10.1175/1520-0493(1989)117%3C1779:ACMFSF%3E2.0.CO;2.

Weisman, M. L., and Coauthors, 2015: The Mesoscale Predictability Experiment (MPEX). *Bull. Amer. Meteor. Soc.*, **96**, 2127–2149, https://doi.org/10.1175/BAMS-D-13-00281.1.

Wick, G. A., and Coauthors, 2020: NOAA's Sensing Hazards with Operational Unmanned Technology (SHOUT) experiment observations and forecast impacts. *Bull. Amer. Meteor. Soc.*, **101**, E968–E987, https://doi.org/10.1175/BAMS-D-18-0257.1.

Zhang, C., Y. Wang, and K. Hamilton, 2011: Improved representation of boundary layer clouds over the southeast Pacific in ARW-WRF using a modified Tiedtke cumulus parameterization scheme. *Mon. Wea. Rev.*, **139**, 3489–3513, https://doi.org/10.1175/MWR-D-10-05091.1.

Zhang, F., C. Snyder, and R. Rotunno, 2002: Mesoscale predictability of the "surprise" snowstorm of 24–25 January 2000. *Mon. Wea. Rev.*, **130**, 1617–1632, https://doi.org/10.1175/1520-0493(2002)130<1617:MPOTSS>2.0.CO;2.

——, N. Bei, R. Rotunno, C. Snyder, and C. C. Epifanio, 2007: Mesoscale predictability of moist baroclinic waves: Convection-permitting experiments and multistage error growth dynamics. *J. Atmos. Sci.*, **64**, 3579–3594, https://doi.org/10.1175/JAS4028.1.

Zhang, X., X.-Y. Huang, and N. Pan, 2013: Development of the upgraded tangent linear and adjoint of the Weather Research and Forecasting (WRF) model. *J. Atmos. Oceanic Technol.*, **30**, 1180–1188, https://doi.org/10.1175/JTECH-D-12-00213.1.

Brought to you by NAVAL RESEARCH LABORATORY | Unauthenticated | Downloaded 02/06/25 06:40 PM UTC